*Supporting Information*

# Controllable Vacancy Strategy Mediated by Organic Ligands of Nickel Fluoride Alkoxides for High-Performance Aqueous Energy Storage

Wei Shi, ‡[a] Zeshuo Meng, ‡[a] Zijin Xu, [a] Jian Xu, [a] Xucong Sun, [a] Haoshan Nan, [a] Chenxu Zhang, [a] Shansheng Yu, *[a] Xiaoying Hu *[b] and Hongwei Tian *[a]

* Corresponding author.

[a] Key Laboratory of Automobile Materials of MOE, School of Materials Science and Engineering, Jilin University, Changchun, 130012, China. E-mail: yuss@jlu.edu.cn, tianhw@jlu.edu.cn.

[b] College of Science and Laboratory of Materials Design and Quantum Simulation, Changchun University, Changchun 130022, China. E-mail: huxy@ccu.edu.cn.

‡ These authors contributed equally to this work.

## Experimental Section

### 1. Chemicals and reagents

$NiCl_2 \cdot 6H_2O$ was purchased from Shanghai Macklin Biochemical Co., Ltd. $NH_4F$ was obtained from Xilong Science Co., Ltd. The urea was provided by Aladdin Industrial Corporation. The solvents ethanol, ethylene glycol, 1-propanol, and 1-butanol were all of analytical grade and purchased from Sinopharm Chemical Reagent Co., Ltd. $K_3[Fe(CN)_6]$, $Bi(NO_3)_3 \cdot 5H_2O$, polyvinylpyrrolidone (PVP), and $HNO_3$ were obtained from Beijing Chemical Works.

### 2. Synthesis of $Ni(OH)_2$

The $Ni(OH)_2$ sample was prepared by hydrolysis of urea. To this end, urea (0.451 g, 7.5 mmol) and $NiCl_2 \cdot 6H_2O$ (0.444g, 1.87 mmol) were first dissolved in 20 ml ethylene glycol solvent (EG). The mixture was transferred to an autoclave and heated at 120 °C for 4 h to complete the reaction. The subsequent sample treatment process was the same as the mentioned above procedure.

### 3. Synthesis of HHP $Bi_2O_3$

The Bi-Fe TBA precursor was first prepared by solution method followed by etching using KOH solution to yield HHP $Bi_2O_3$.[1] Specifically, 100 ml aqueous solution containing $K_3[Fe(CN)_6]$ (0.332 g) was added dropwise to 100 ml water and ethanol containing $Bi(NO_3)_3 \cdot 5H_2O$ (0.488 g), polyvinylpyrrolidone (PVP) (3.0 g), and $HNO_3$ (5 mL). The Bi-Fe TBA precursor was obtained after standing still at room temperature for 12 h. Next, Bi-Fe TBA precursor (10 mg) was added to 10 ml of KOH (0.05 g) solution and stirred for 2 h to obtain the HHP $Bi_2O_3$ sample.

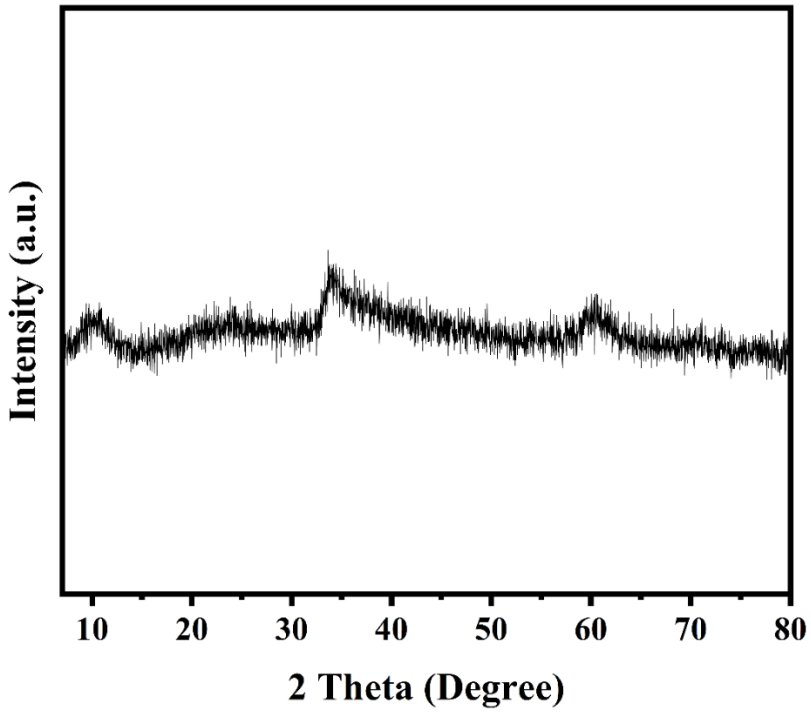


`

**Figure S1.** XRD patterns of $Ni(OH)_2$ samples.

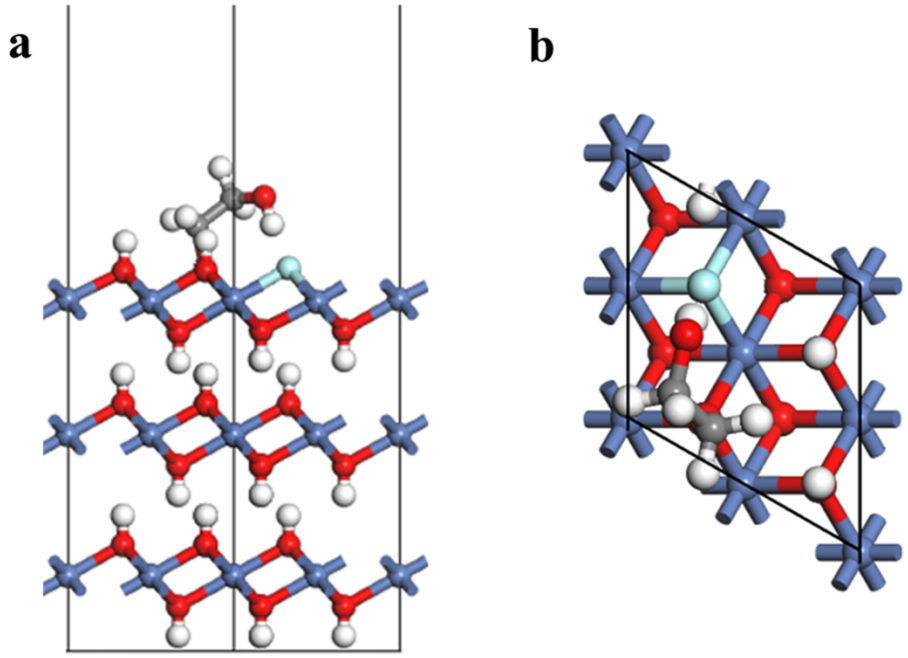


**Figure S2.** (a) Test plot and (b) top view of the structural computational model.

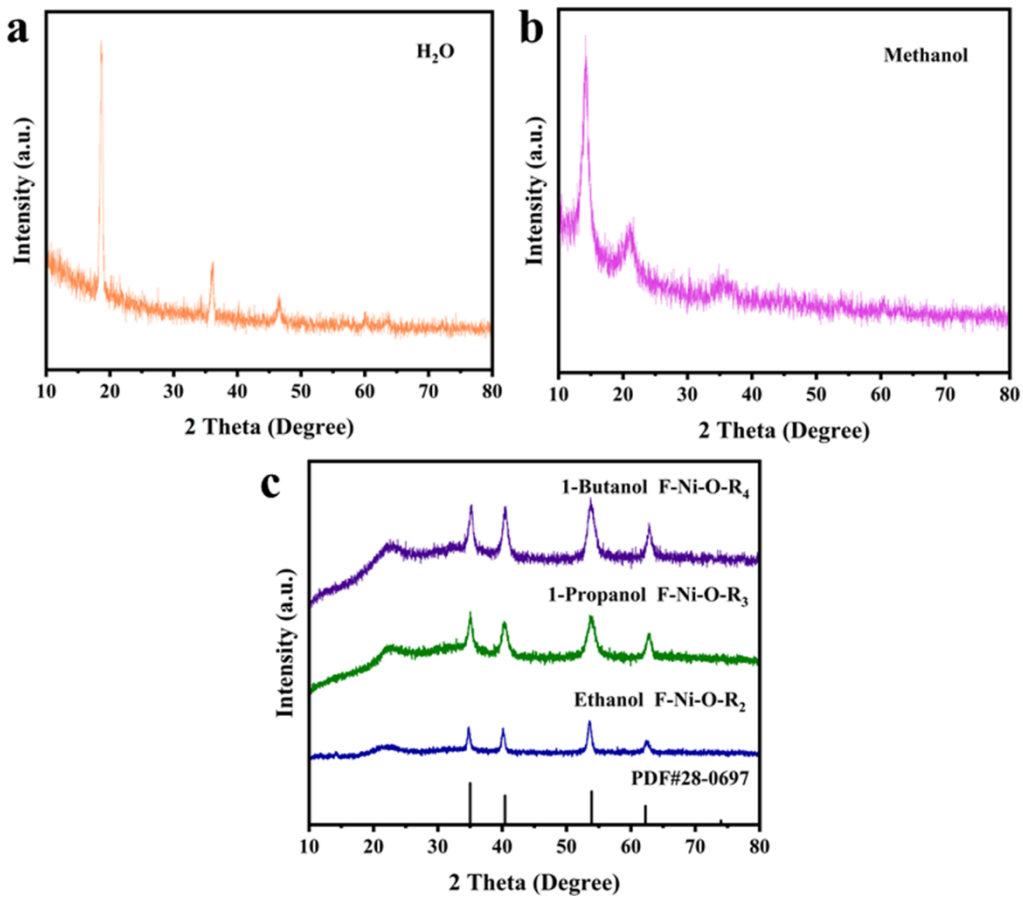


**Figure S3.** XRD patterns of the samples synthesized in (a) $H_2O$, (b) methanol, (c) 1-propanol, and 1-butanol solvents.

The XRD profiles of prepared samples using water without carbon chains and methanol with shorter carbon chain solvents under other unchanged experimental conditions are shown in **Figure S3**(a) and (b), respectively. Obviously, the diffraction peaks did not depict the crystal structural features of F-Ni-$O_2$-$R_2$, indicating failed synthesis. However, samples synthesized in alcohol solvents composed of carbon chains with two C atoms or more showed different XRD patterns (**Figure S3**(c)). Therefore, this method showed good universality with mechanism equations that can be expressed by Equations (1)-(3):

$$NiCl_2 \rightarrow Ni^{2+} + 2Cl^- \tag{1}$$

$$NH_4F \rightarrow NH_4^+ + F^- \tag{2}$$

$$Ni^{2+} + (x+1)F^- + H_x{-}O_x{-}R_y \rightarrow F{-}Ni{-}O_x{-}R_y + xHF \tag{3}$$

The structural calculation of F-Ni-$O_2$-$R_2$ synthesized with ethylene glycol solvent (Figure 1a) revealed a distance between the H element at the end of the carbon chain and the F element

of 1.682 Å. This value fitted well the distance range of hydrogen bonding. Therefore, hydrogen bonds were formed between the H and F atoms, and the mechanism of hydrogen bonding for stabilizing the structure could be deduced. In fact, $Ni(OH)_2$ could stably exist due to the strong ionic bond between $Ni^{2+}$ and $OH^-$ ions. As a single ion, $F^-$ exhibited extremely strong electronegativity, but still displayed relatively weak electronegativity compared to $OH^-$. The decrease in the electron attraction ability relative to $OH^-$ rendered Ni-F bond less strong than that of Ni-OH, making it difficult to maintain the corresponding structure. However, the electron cloud of $F^-$ shifted to the direction of the carbon chain after the introduction of hydrogen bonds, while $F^-$ for $Ni^{2+}$ side exhibited enhanced electropositivity. This caused the electron cloud of $Ni^{2+}$ to move towards the $F^-$ side, resulting in relatively stable structure. Therefore, hydrogen bonds can be generated to stabilize the structure for carbon chains with a length greater than or equal to 2, forming the corresponding F-Ni-$O_x$-$R_y$ structure. The two phases of F-Ni-OH and F-Ni-OR could not be synthesized as expected using water and methanol, confirming the importance of introducing organic ligand structures and generating hydrogen bonds for structural stability.

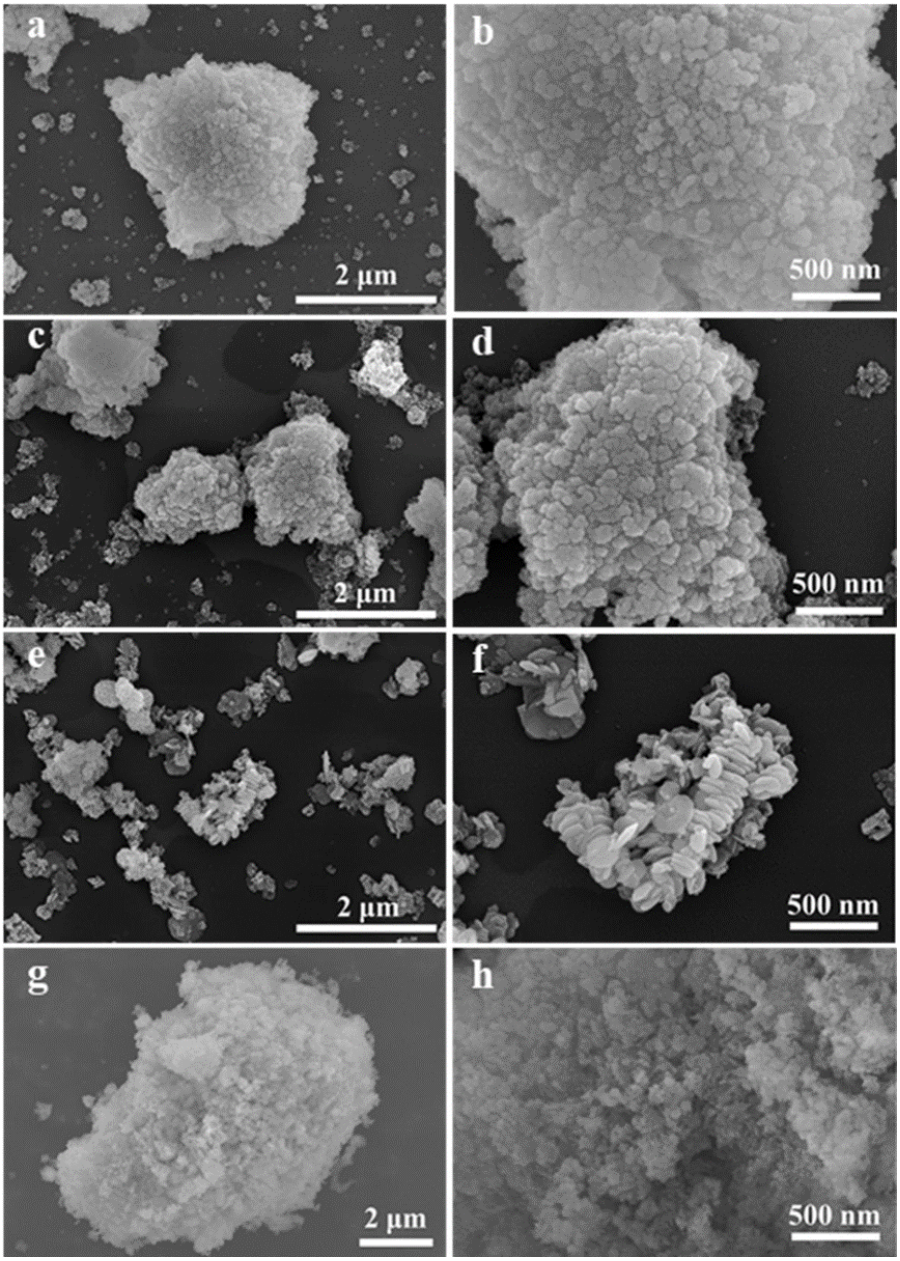


**Figure S4.** SEM images (a, b) of F-Ni-O-$R_2$, (c, d) F-Ni-O-$R_3$, (e, f) F-Ni-O-$R_4$, and (g, h) $Ni(OH)_2$.

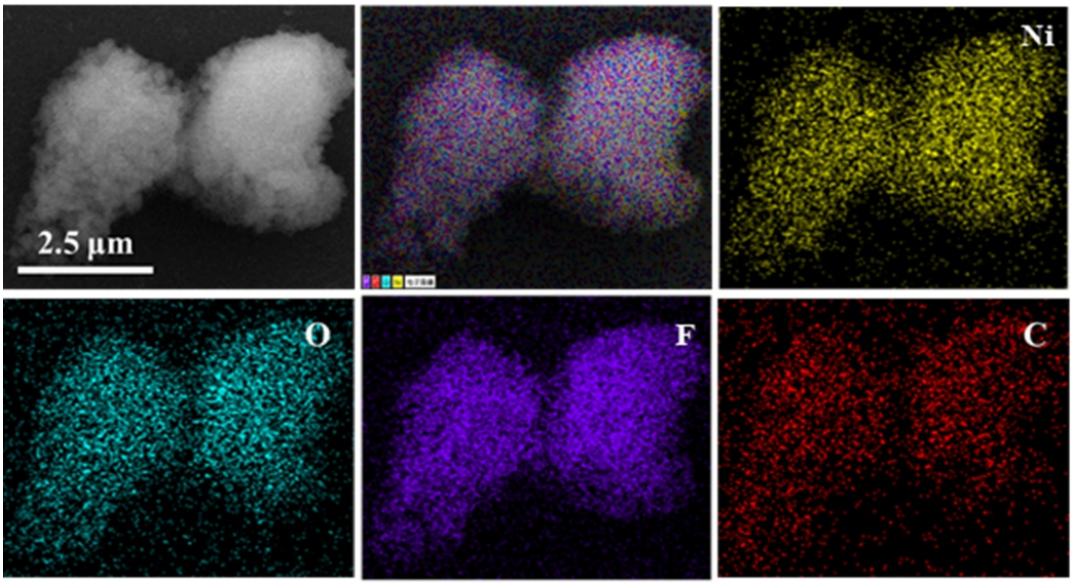


**Figure S5.** The energy dispersion spectra (EDS) mapping images of F-Ni-$O_2$-$R_2$ sample.

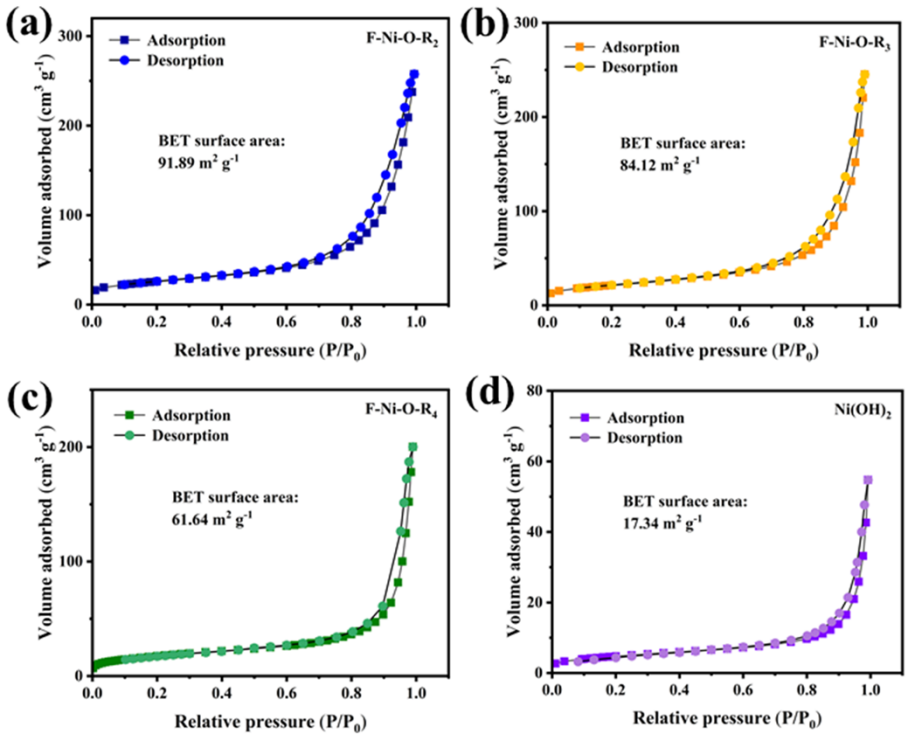


**Figure S6.** Nitrogen sorption isotherms of (a) F-Ni-O-$R_2$, (b) F-Ni-O-$R_3$, (c) F-Ni-O-$R_4$, and (d) $Ni(OH)_2$.

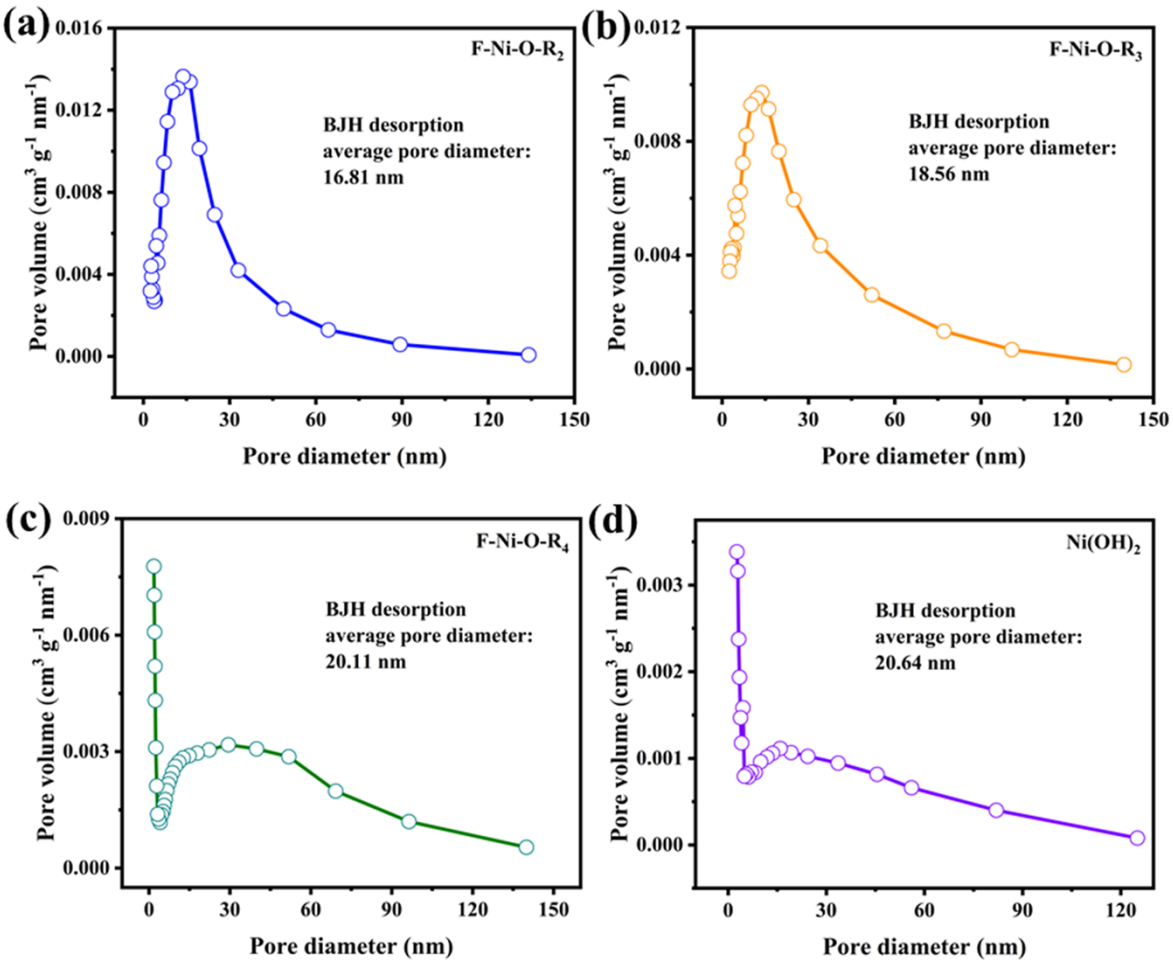


**Figure S7.** Pore size distributions of synthetic samples.

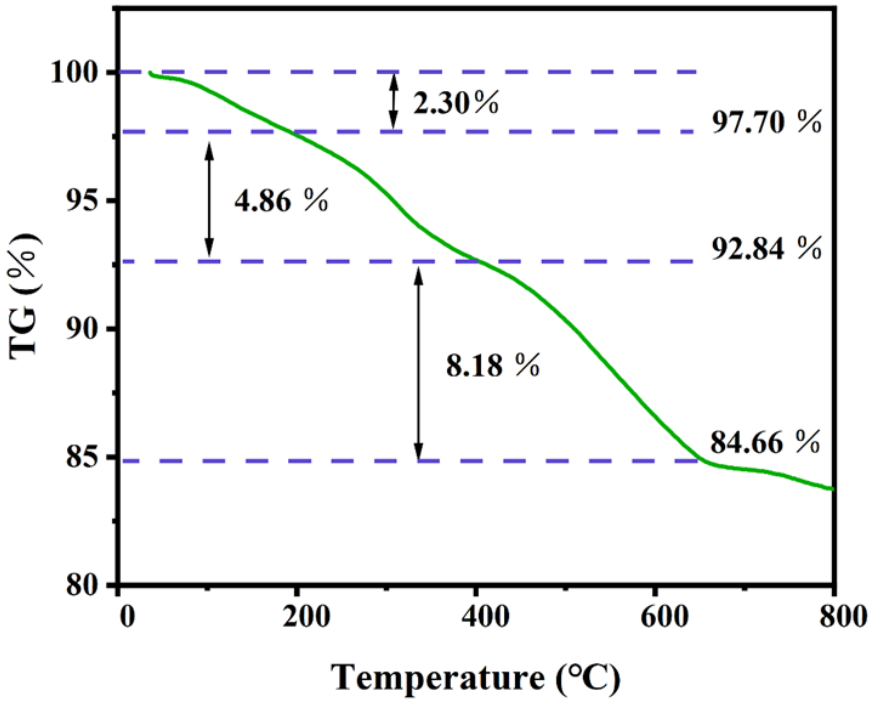


**Figure S8.** TGA curve of F-Ni-$O_2$-$R_2$ sample.

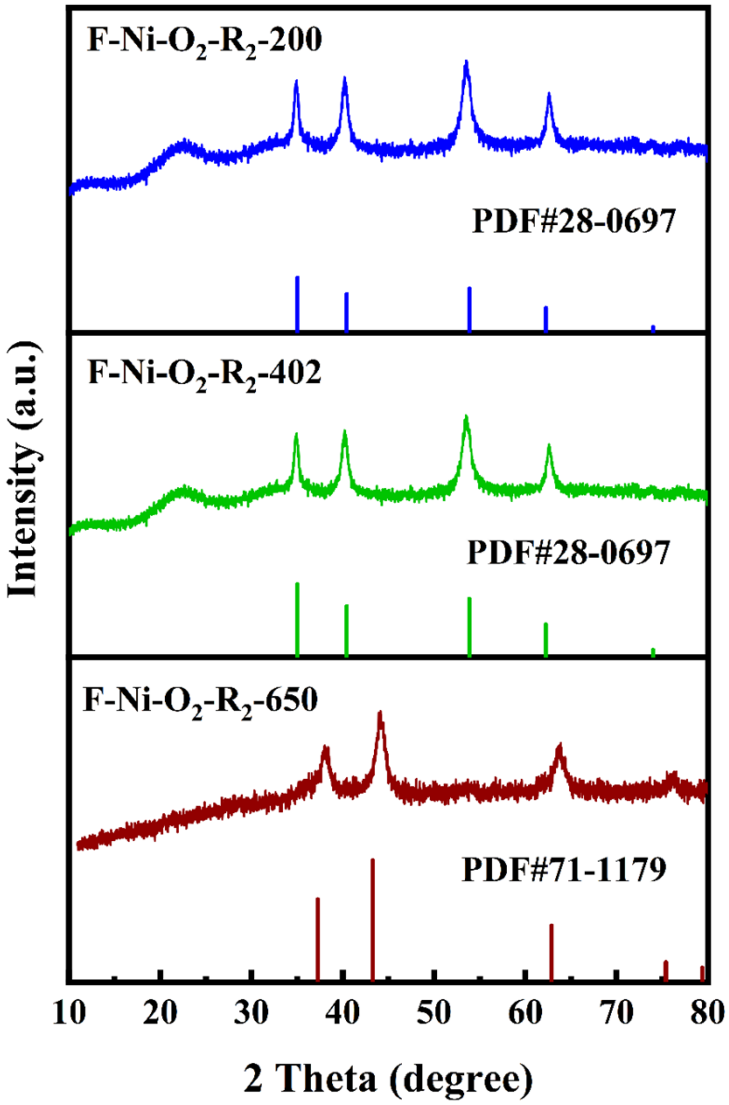


**Figure S9.** XRD patterns corresponding to different temperature stages in TGA of F-Ni-$O_2$-$R_2$ sample.

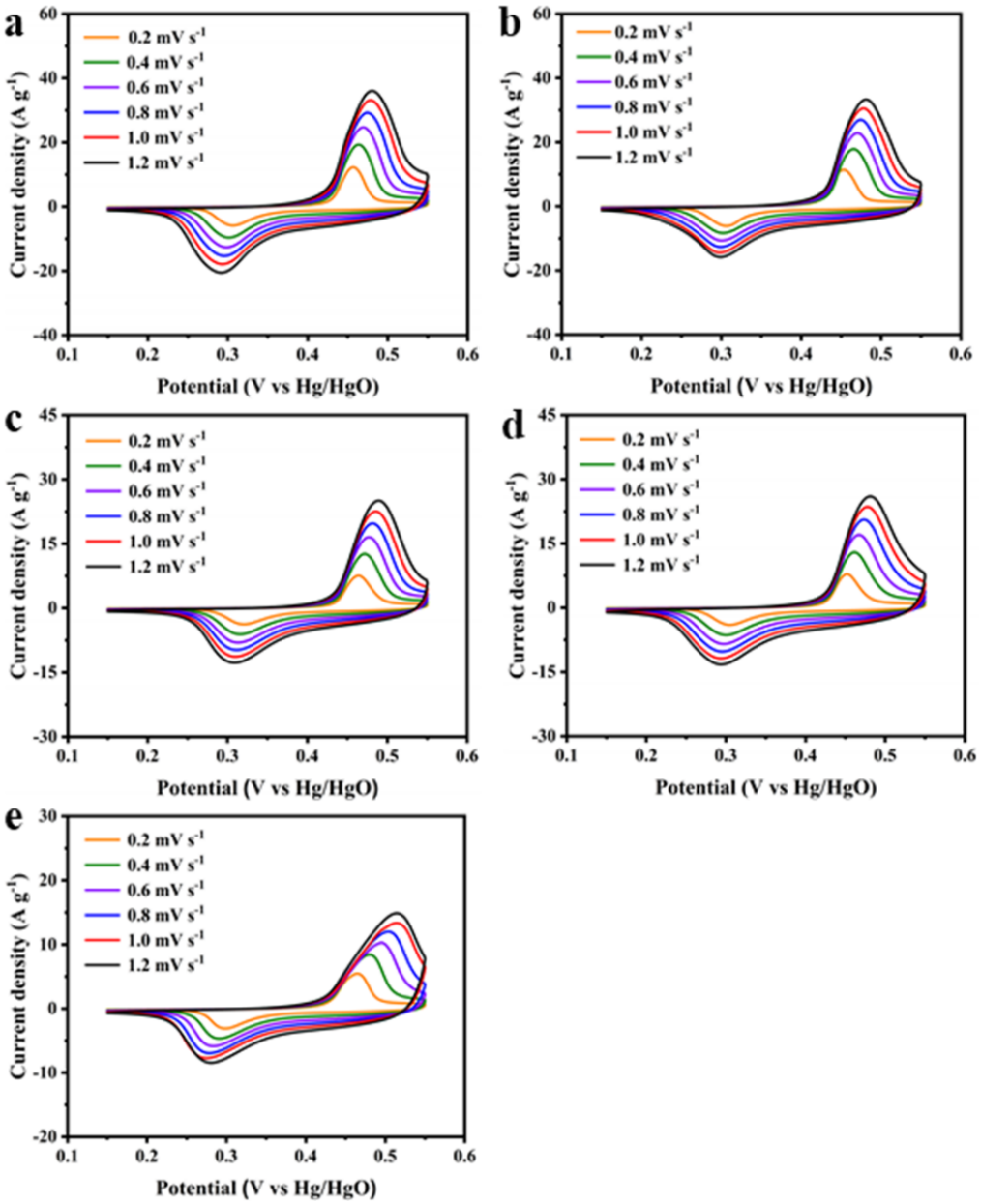


**Figure S10.** CV plots at 0.2-1.2 mV $s^{-1}$ of (a) F-Ni-$O_2$-$R_2$ electrode, (b) F-Ni-O-$R_2$ electrode, (c) F-Ni-O-$R_3$ electrode, (d) F-Ni-O-$R_4$ electrode, and (e) $Ni(OH)_2$ electrode.

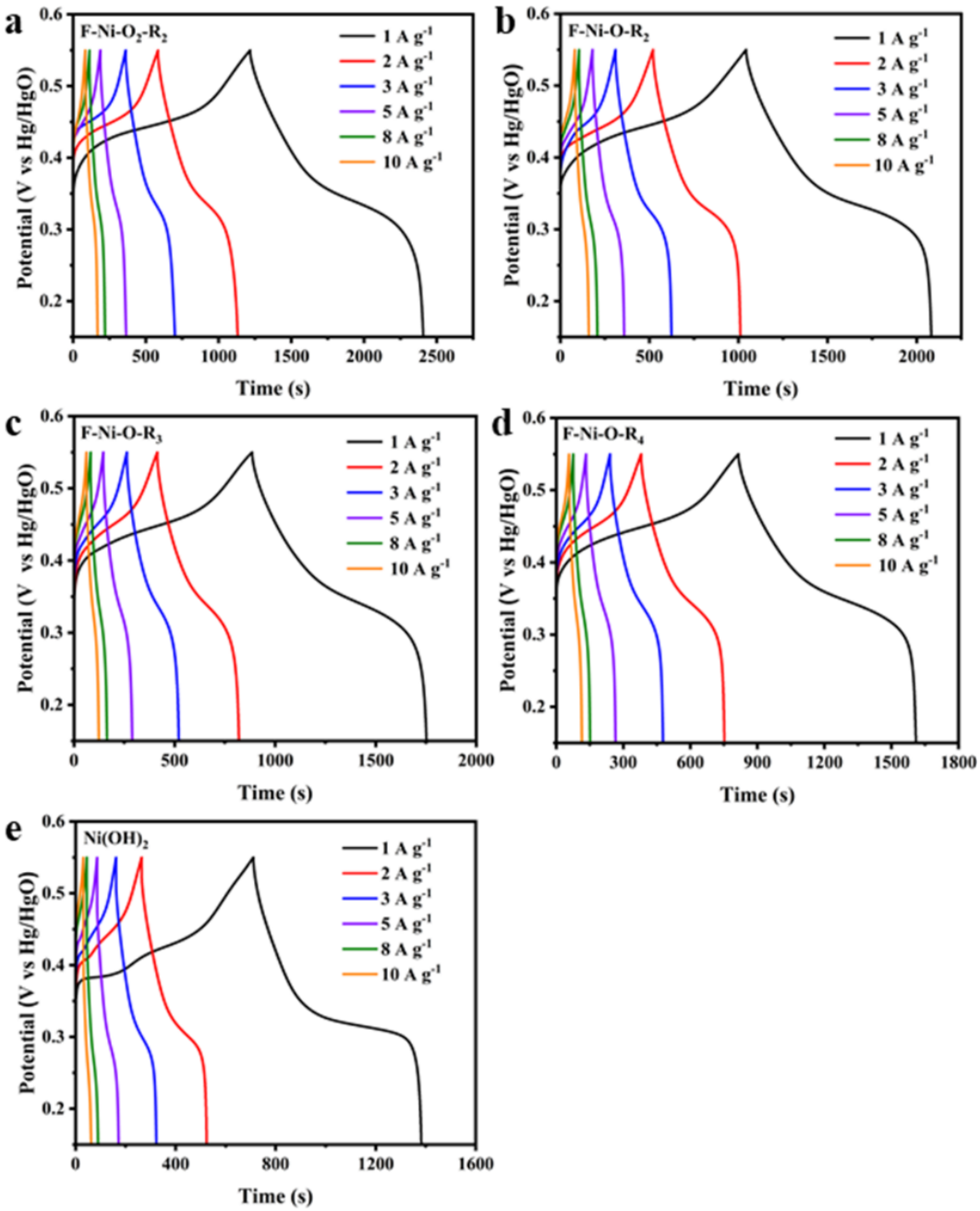


**Figure S11.** GCD curves at 1-10 A $g^{-1}$ of (a) F-Ni-$O_2$-$R_2$ electrode, (b) F-Ni-O-$R_2$ electrode, (c) F-Ni-O-$R_3$ electrode, (d) F-Ni-O-$R_4$ electrode, and (e) $Ni(OH)_2$ electrode.

| | |
|---|---|
| F-Ni-$O_2$-$R_2$ | 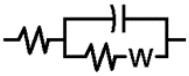 |
| F-Ni-O-$R_2$ | 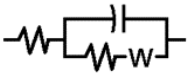 |
| F-Ni-O-$R_3$ | 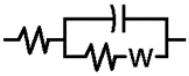 |
| F-Ni-O-$R_4$ | 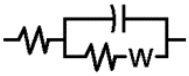 |
| $Ni(OH)_2$ | 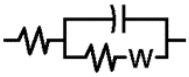 |

**Figure S12.** The fitting equivalent circuit models of prepared candidate electrodes.

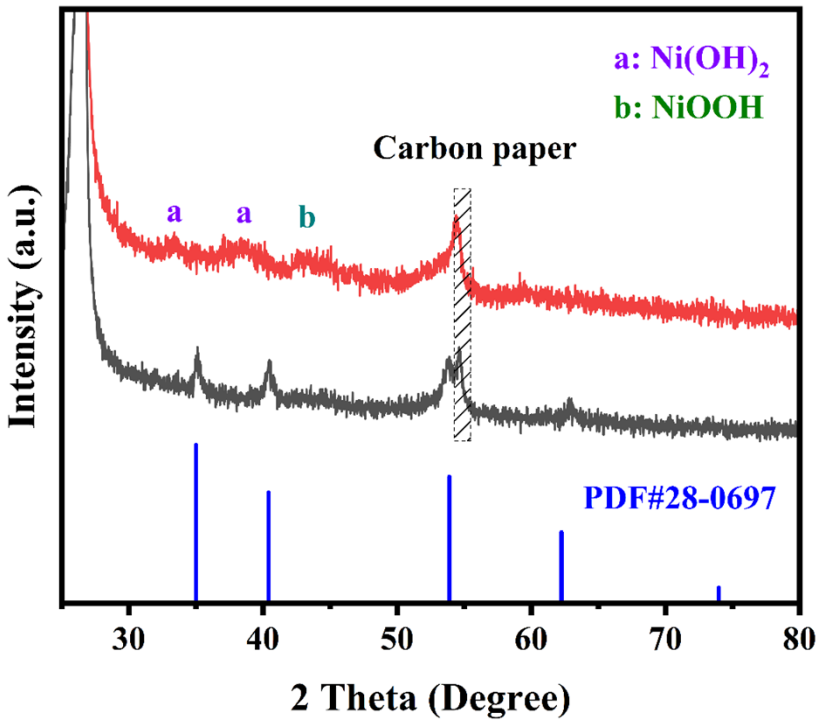


**Figure S13.** XRD patterns of F-Ni-$O_2$-$R_2$ sample loaded on carbon paper before and after preactivation ($Ni(OH)_2$ and NiOOH referenced to PDF#73-1520 and PDF#06-0075 cards, respectively).

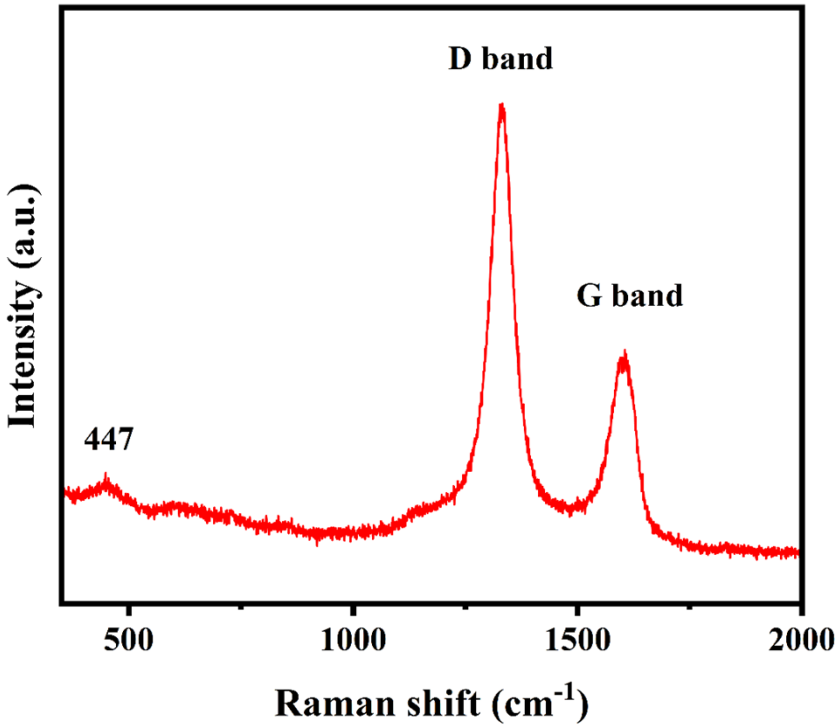


**Figure S14.** Raman pattern of F-Ni-$O_2$-$R_2$ sample after preactivation.

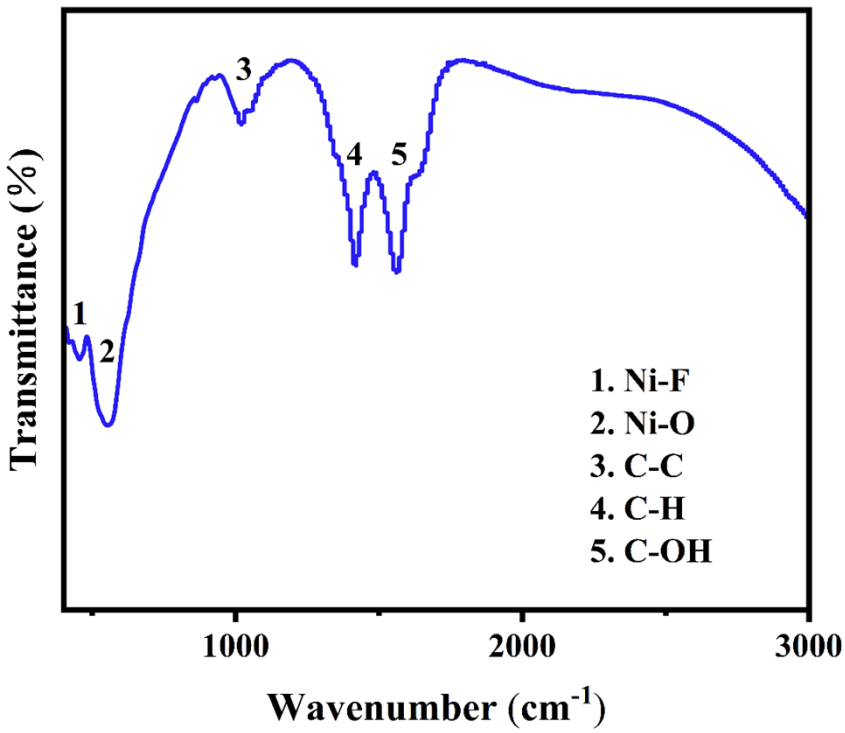


**Figure S15.** IR spectrum of F-Ni-$O_2$-$R_2$ sample after preactivation.

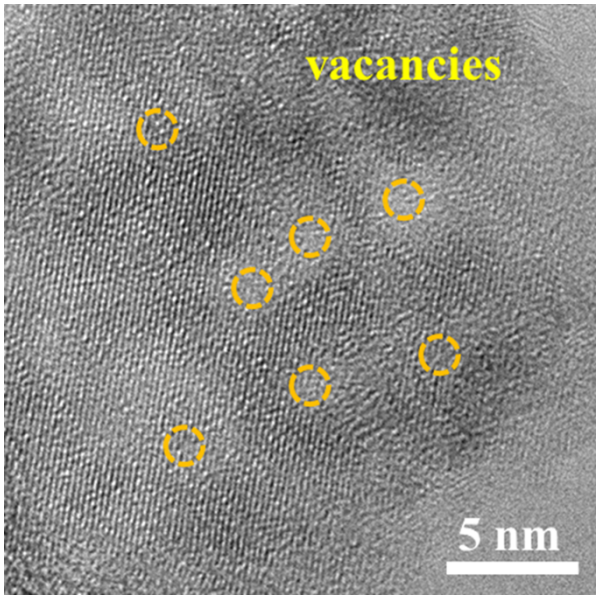


**Figure S16.** HRTEM image of F-Ni-$O_2$-$R_2$ samples after preactivation.

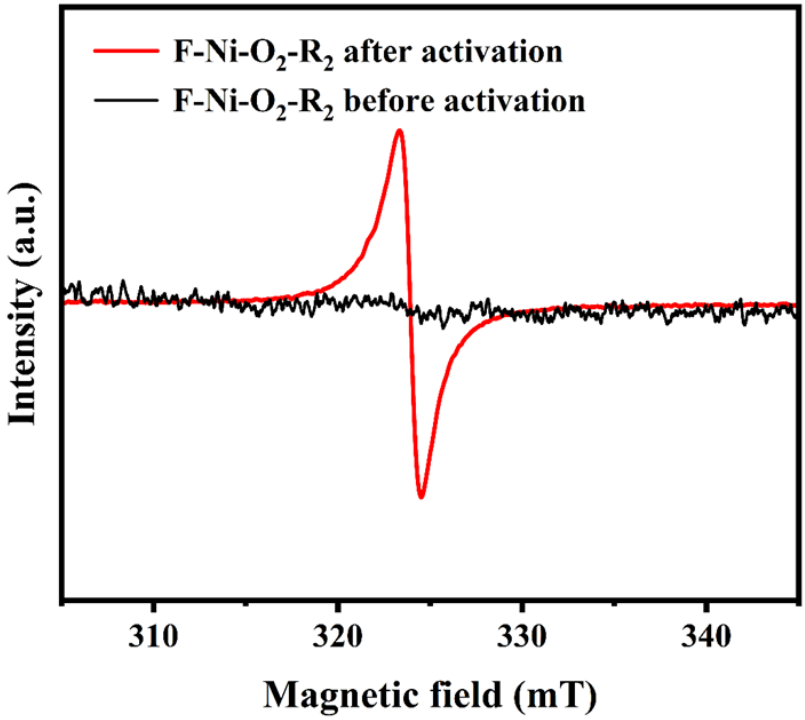


**Figure S17.** Comparison of EPR signals of F-Ni-$O_2$-$R_2$ samples before and after activation.

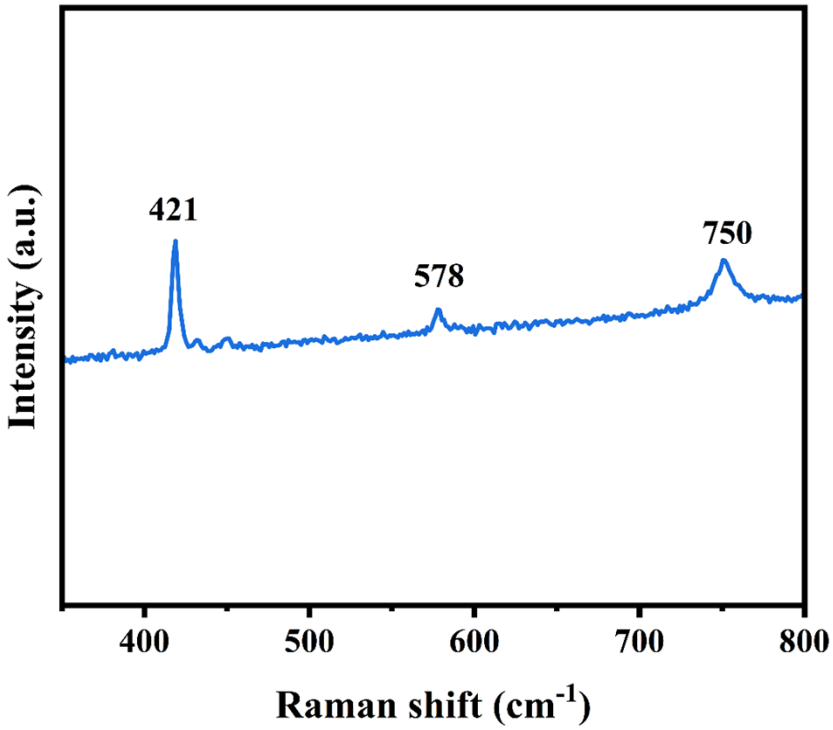


**Figure S18.** Raman spectrum of F-Ni-$O_2$-$R_2$ sample in the initial state.

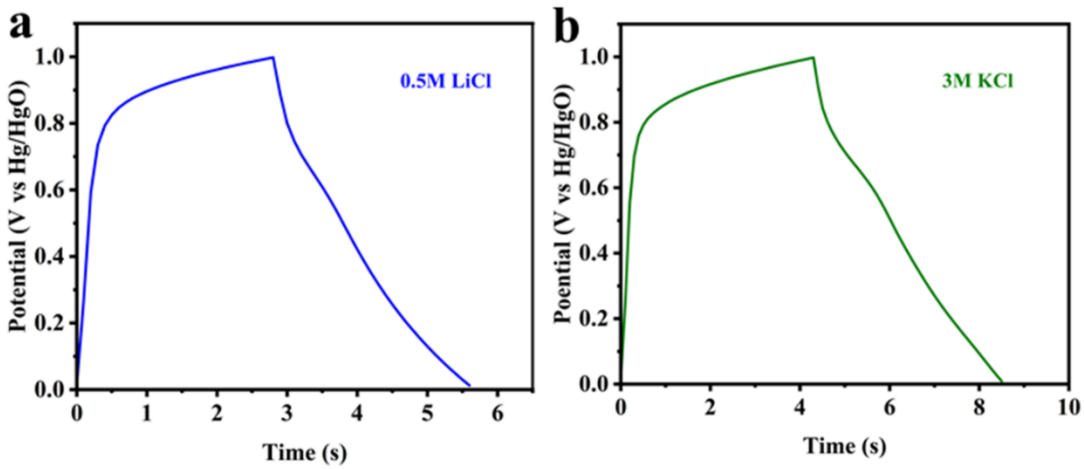


**Figure S19.** GCD curves at 2 A $g^{-1}$ of F-Ni-$O_2$-$R_2$ electrode in neutral electrolyte: (a) 0.5 M LiCl and (b) 3 M KCl.

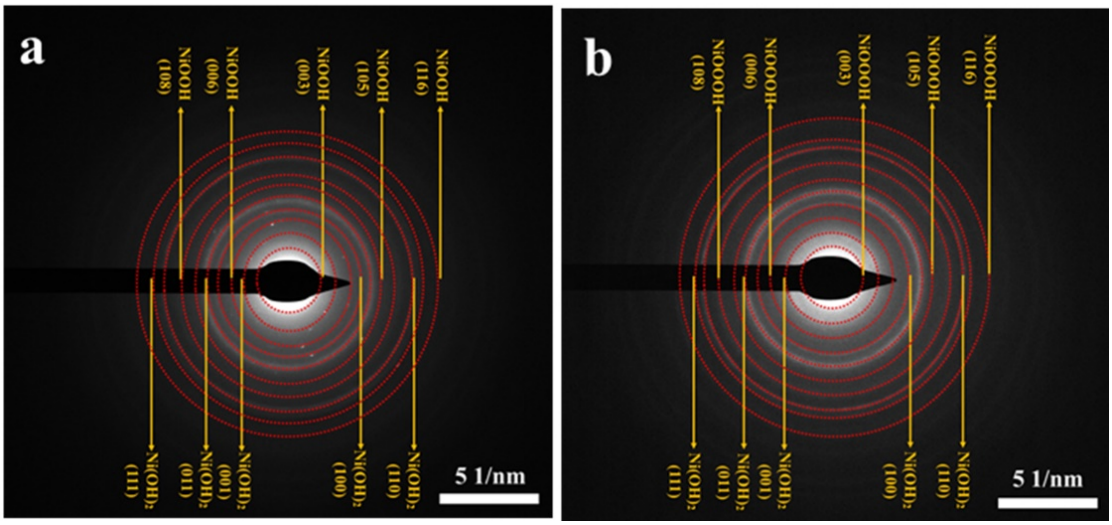


**Figure S20.** SAED patterns of F-Ni-$O_2$-$R_2$ electrode in fully charged (a) and discharged (b) states after preactivation.

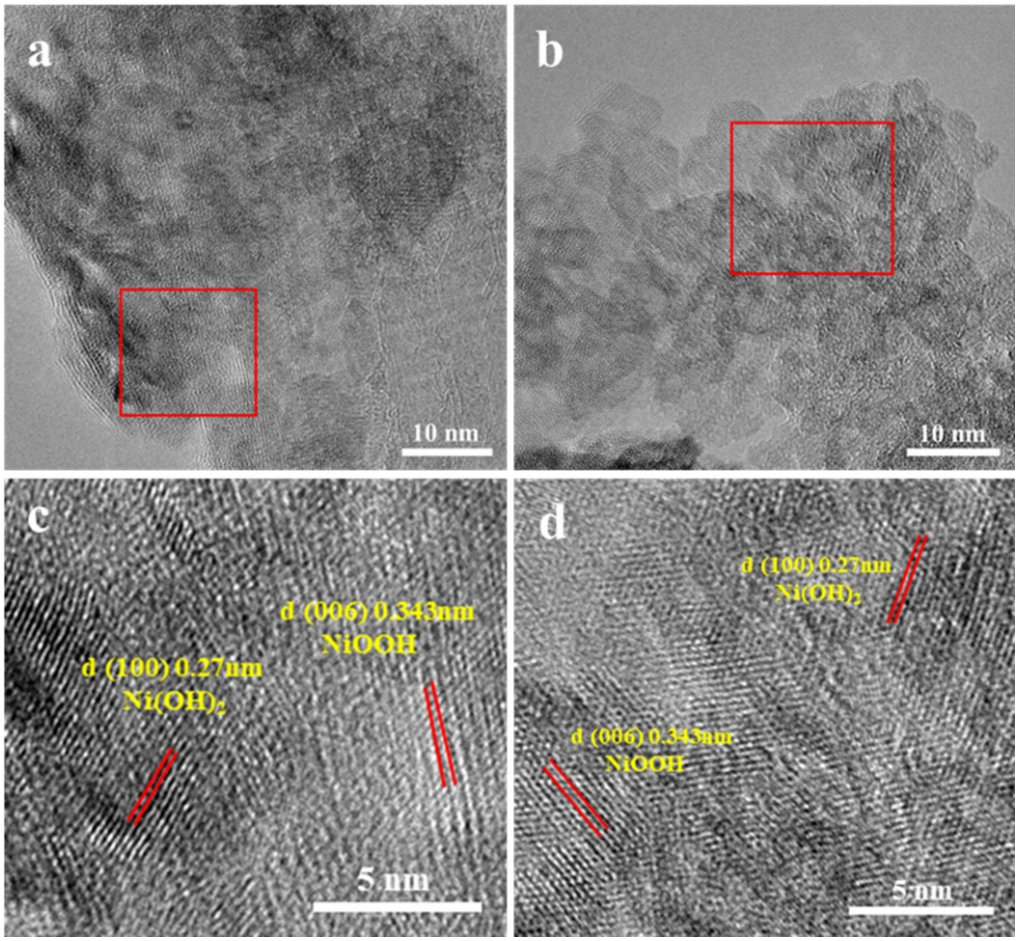


**Figure S21.** *Ex-situ* HRTEM patterns of F-Ni-$O_2$-$R_2$ electrode in fully charged (a) and discharged (b) states after preactivation. (c) and (d) Selected areas in (a) and (b), respectively.

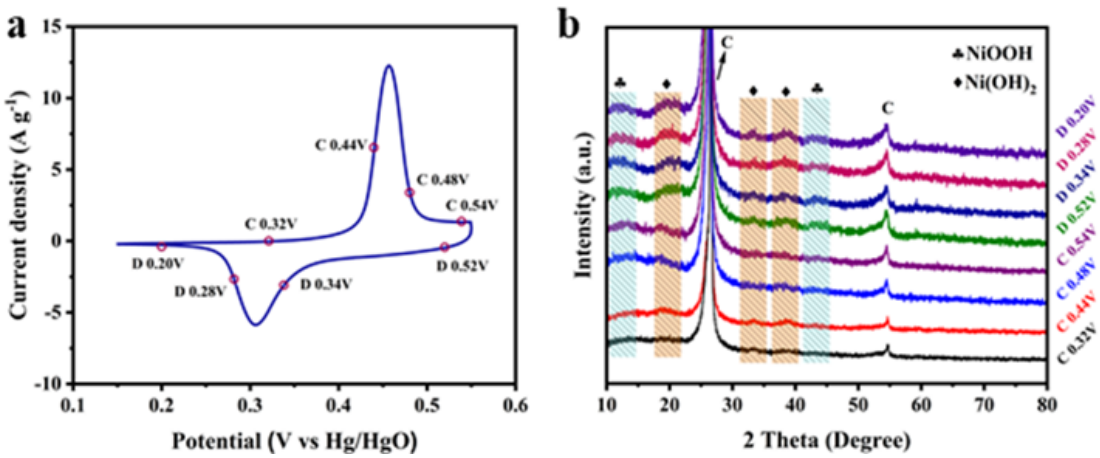


**Figure S22.** (a) CV curve at 0.2 mV $s^{-1}$ of F-Ni-$O_2$-$R_2$ after preactivation. (b) *Ex-situ* XRD patterns of F-Ni-$O_2$-$R_2$ derivatives with different discharge/charge states, corresponding to the redox peak positions in (a).

*Ex-situ* XRD was performed to obtain structural information of the generated species. As shown in **Figure S22**(a), the valence state changes of nickel in CV curve during charge were recorded as 0.32, 0.44, 0.48, and 0.54 V (denoted as Cx, where x is the charging voltage), while the values during discharge were 0.52, 0.34, 0.28, and 0.20 V (denoted as Dy, where y is the discharge voltage). In **Figure S22**(b), the original $Ni_4OHF_7$ signal completely disappeared after preactivation of F-Ni-$O_2$-$R_2$ electrode and replaced by the new peak signals of NiOOH and $Ni(OH)_2$. In addition, the signal of NiOOH during the charging process (potential range 0.32 V-0.54 V) showed an increasing trend, indicating the gradual conversion of $Ni(OH)_2$ to NiOOH. At voltage exceeding 0.55 V and the start of discharge stage, the characteristic peaks related to $Ni(OH)_2$ became more obvious to complete the reversible phase transition of the energy storage process.

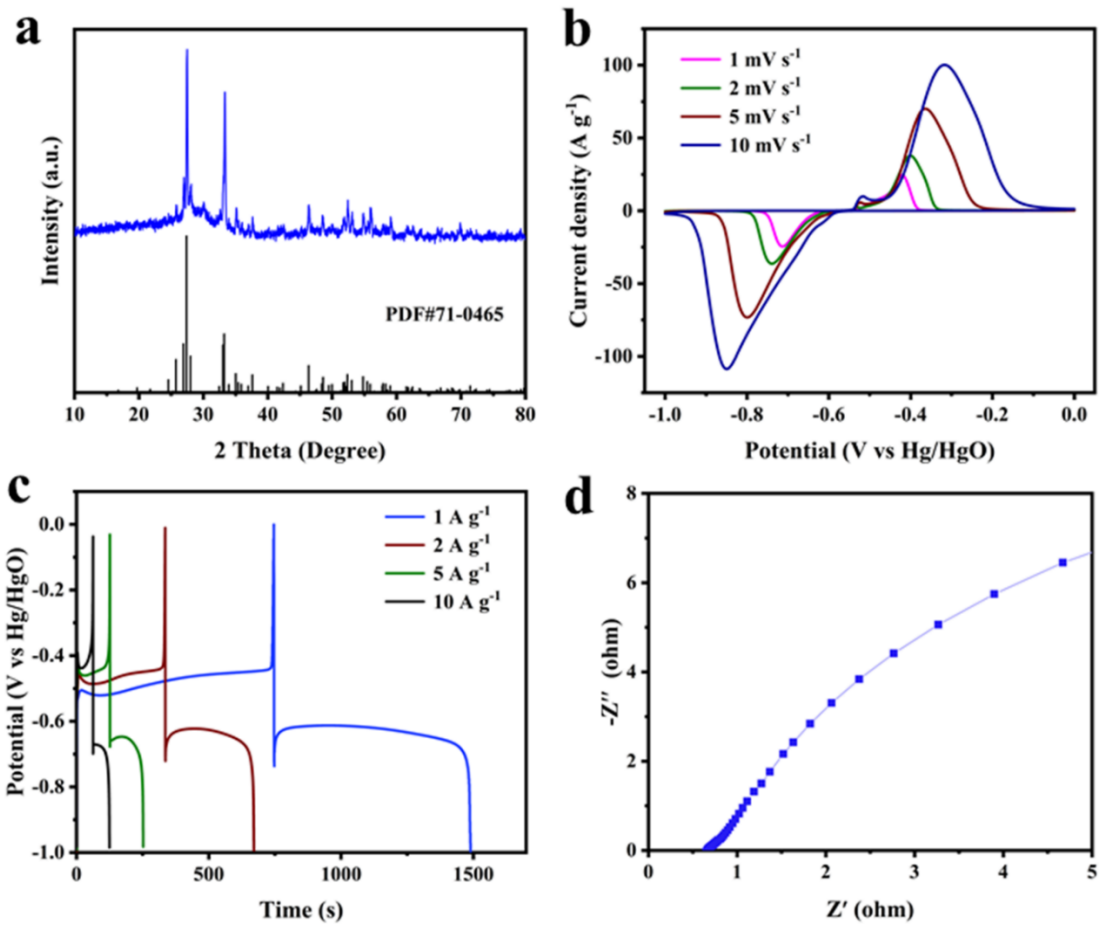


**Figure S23.** (a) XRD patterns of synthesized HHP $Bi_2O_3$ sample, (b) CV plots at 1-10 mV $s^{-1}$, (c) GCD curves at 1-10 A $g^{-1}$, and (d) Nyquist plots of HHP $Bi_2O_3$ electrode.

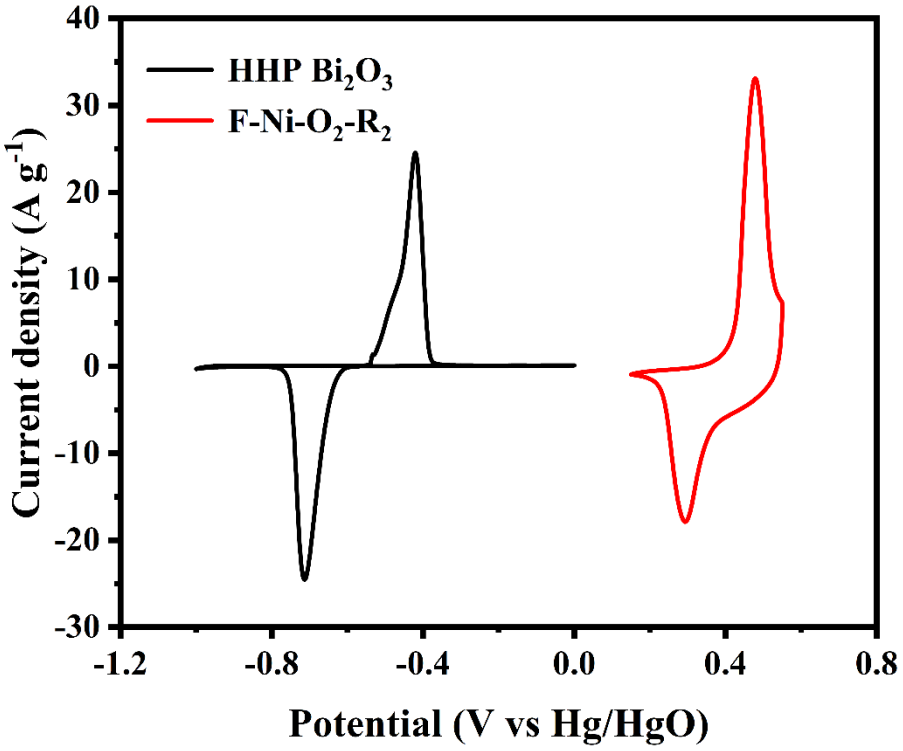


**Figure S24.** CV curves of F-Ni-$O_2$-$R_2$ and HHP $Bi_2O_3$ electrodes at the scan rate of 1 mV $s^{-1}$.

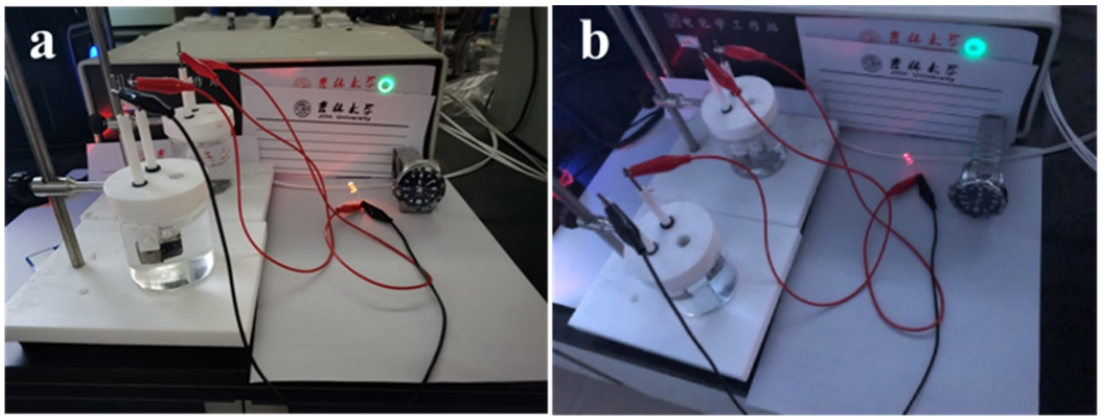


**Figure S25.** The energy storage device assembled by two sets of F-Ni-$O_2$-$R_2$//HHP $Bi_2O_3$. (a) Device starts to light the LED bulb. (b) Device continues to supply power to the LED bulb after 30 min.

**Supplemental tables**

**Table S1.** The crystalline parameters of F-Ni-$O_2$-$R_2$ and $Ni(OH)_2$.

| Sample | PDF card | Crystal system | Space group | Cell(a×b×c) Å |
|---|---|---|---|---|
| F-Ni-$O_2$-$R_2$ | 28-0697 | hexagonal | P-3m1 (164) | 2.973×2.973×4.598 |
| $Ni(OH)_2$ | 73-1520 | hexagonal | P-3m1 (164) | 3.114×3.114×4.617 |
| $Ni(OH)_2$ | 14-0117 | hexagonal | P-3m1 (164) | 3.126×3.126×4.605 |

**Table S2.** Diffraction peak positions and corresponding crystal planes in XRD profiles.

| 2 Theta | 35.1° | 40.4° | 53.9° | 63.0° | 72.3° | 74.2° | 77.0° | 87.5° | 95.5° |
|---|---|---|---|---|---|---|---|---|---|
| Crystal planes | (100) | (011) | (012) | (110) | (103) | (200) | (112) | (202) | (104) |

**Table S3.** Comparison of the capacitance obtained in this work with reported values.

| Electrode | Electrolyte | Specific capacitance | Reference |
|---|---|---|---|
| F-Ni-$O_2$-$R_2$ | 3 M KOH + 0.5 M LiOH | 2975.0 F $g^{-1}$ at 1 A $g^{-1}$ | This work |
| NiCoMoS@LDH/NF | 3 M KOH | 2968.8 F $g^{-1}$ at 1 A $g^{-1}$ | 2 |
| Ni-MOFs/$V_2CT_x$-MXene | 1 M KOH | 2453 F $g^{-1}$ at 1 A $g^{-1}$ | 3 |
| F-CoNi-A | 1 M KOH | 2476.0 F $g^{-1}$ at 1 A $g^{-1}$ | 4 |
| NiCoP@C@$Ni(OH)_2$ | 3 M KOH | 2300.8 F $g^{-1}$at 1 A $g^{-1}$ | 5 |
| Ni-HF | 2 M KOH | 2030.3 F $g^{-1}$ at 1 A $g^{-1}$ | 6 |
| Co-Zn(OH)F | 2 M KOH | 1970.0 F $g^{-1}$ at 1 A $g^{-1}$ | 7 |
| NiCoP-CoP | 2 M KOH | 1969 F $g^{-1}$ at 1 A $g^{-1}$ | 8 |
| $KNiF_3$@CNTs-8 | 3 M KOH + 0.5 M LiOH | 1642.8 F $g^{-1}$ at 1 A $g^{-1}$ | 9 |
| Al-Co(OH)F | 2 M KOH | 1576 F $g^{-1}$ at 1 A $g^{-1}$ | 10 |
| Co-Ni-B-S | 6 M KOH | 1281 F $g^{-1}$ at 1 A $g^{-1}$ | 11 |
| $CoNiO_2$-Ar | 6 M KOH | 1172.6 F $g^{-1}$ at 1 A $g^{-1}$ | 12 |
| $Ni_3Co_1WO_4$/HPC | 6 M KOH | 1084 F $g^{-1}$ at 1 A $g^{-1}$ | 13 |
| $Ti_3C_2$/Ni-Co-Al-LDH | 1 M KOH | 748.2 F $g^{-1}$ at 1 A $g^{-1}$ | 14 |

**Table S4.** The specific capacitances under current densities of 1-10A $g^{-1}$.

| Electrode | Specific capacitance (F $g^{-1}$) | | | | | |
|---|---|---|---|---|---|---|
| | 1 A $g^{-1}$ | 2 A $g^{-1}$ | 3 A $g^{-1}$ | 5 A $g^{-1}$ | 8 A $g^{-1}$ | 10 A $g^{-1}$ |
| F-Ni-$O_2$-$R_2$ | 2975.0 | 2735.0 | 2533.5 | 2216.3 | 2136.0 | 2107.5 |
| F-Ni-O-$R_2$ | 2610.0 | 2451.5 | 2355.0 | 2222.5 | 2066.0 | 1960.0 |
| F-Ni-O-$R_3$ | 2167.0 | 2030.0 | 1939.5 | 1798.8 | 1636.0 | 1537.5 |
| F-Ni-O-$R_4$ | 2015.0 | 1860.0 | 1776.8 | 1662.5 | 1514.0 | 1425.0 |
| $Ni(OH)_2$ | 1680.0 | 1300.0 | 1207.5 | 1075.0 | 898.0 | 777.5 |

**Table S5.** Fitting results of prepared electrodes obtained from the EIS curves.

| Electrode | Rs (Ω) | Rct (Ω) | Cdl (F) | W (Yo, S·$sec^{0.5}$) |
|---|---|---|---|---|
| F-Ni-$O_2$-$R_2$ | 0.6459 | 0.4656 | $1.52\times10^{-3}$ | 0.07463 |
| F-Ni-O-$R_2$ | 0.7017 | 0.5270 | $1.21\times10^{-3}$ | 0.5635 |
| F-Ni-O-$R_3$ | 0.6881 | 1.679 | $2.52\times10^{-3}$ | 0.5850 |
| F-Ni-O-$R_4$ | 0.9383 | 2.277 | $7.00\times10^{-5}$ | 0.3761 |
| $Ni(OH)_2$ | 0.7545 | 3.919 | $1.965\times10^{-3}$ | 0.3157 |

**Table S6.** Comparison of resistivity test results of F-Ni-$O_2$-$R_2$ before preactivation and F-Ni-$O_2$-$R_2$ after preactivation.

| Sample | Resistivity (Ω·m) | Conductivity (S/m) |
|---|---|---|
| F-Ni-$O_2$-$R_2$ before preactivation | 6.4202 | 0.1558 |
| | 6.3394 | 0.1577 |
| F-Ni-$O_2$-$R_2$ after preactivation | 0.5738 | 1.7428 |
| | 0.5594 | 1.7876 |

**Table S7.** Comparison of the performance of assembled F-Ni-$O_2$-$R_2$//HHP $Bi_2O_3$ device with others reported in the literature.

| Aqueous energy storage devices | Potential Window (V) | Energy density (Wh $kg^{-1}$) | power density (W $kg^{-1}$) | Reference |
|---|---|---|---|---|
| F-Ni-$O_2$-$R_2$//HHP $Bi_2O_3$ | 0-1.6 V | 55.1-127.6 | 800-32000 | This work |
| $Bi_2O_3$/$Bi_2Se_3$ NFs//$NiCoSe_2$/$Ni_{0.85}Se$ NP | 0-1.6 V | 43.6-88.4 | 2400-32000 | 15 |
| N-GNTs@$O_V$-$Bi_2O_3$ NSAs//N-GNTs@$CoNi_2S_4$ NP | 0-1.6 V | 51.3-86.6 | 1600-24000 | 16 |
| Ni – Zn – Co – S-0.33 NSAs/NF//$Bi_2O_3$/NF | 0-1.6 V | 66.9-91.7 | 458-6696 | 17 |
| $Ni_xCo_{1-x}$ $(OH)_2$//$Bi_2O_3$ | 0-1.6 V | 37.0-66.0 | 356-6439 | 1 |
| $Ni(OH)_2$//$(BiO)_4CO_3(OH)_2$ | 0-1.6 V | 27.3-92.0 | 27.3-670 | 18 |
| ESCNF@$Bi_2O_3$//CF@$NiCo_2O_4$ | 0-1.9 V | 18.0-25.1 | 786.2-2949 | 19 |
| Bi//10#/Ag(37%) | 0-1.6 V | 3.8-25.4 | 400-2800 | 20 |

**Table S8.** Comparison of the performance of F-Ni-$O_2$-$R_2$//AC asymmetric supercapacitor with other Ni-based ASC devices reported in the literature.

| ASC devices | Potential Window (V) | Energy density (Wh $kg^{-1}$) | power density (W $kg^{-1}$) | Reference |
|---|---|---|---|---|
| F-Ni-$O_2$-$R_2$//AC | 0-1.6 V | 29.1-64.6 | 800-32000 | This work |
| CoP/NiCoP//AC | 0-1.6 V | 28.4-51.6 | 800-12000 | 21 |
| NiMn-LDH//AC | 0-1.6 V | 16.9-46.7 | 1700-13500 | 22 |
| $MnCo_2O_4$@Ni(OH) //AC | 0-1.6 V | 7.26-48 | 1400-14900 | 23 |
| MnCo-LDH@$Ni(OH)_2$//AC | 0-1.5 V | 9.8-47.9 | 750.7-5020.5 | 24 |
| $Ni(OH)_2$//AC | 0-1.3 V | 12.6-35.7 | 490-1670 | 25 |

## References


1 G. Zan, T. Wu, P. Hu, Y. Zhou, S. Zhao, S. Xu, J. Chen, Y. Cui and Q. Wu, *Energy Stor. Mater.*, 2020, **28**, 82-90.

2 K. Zhang, H.-Y. Zeng, M.-X. Wang, H.-B. Li, W. Yan, H.-B. Wang and Z.-H. Tang, *J. Mater. Chem. A*, 2022, **10**, 11213-11224.

3 X. Yang, Y. Tian, S. Li, Y.-P. Wu, Q. Zhang, D.-S. Li and S. Zhang, *J. Mater. Chem. A*, 2022, **10**, 12225-12234.

4 M. Chu, Q. Xu, S. Chen, Y. Hu, H. Jiang and C. Li, *Chem. Eng. Sci.*, 2021, **240**, 116649.

5 Q. Zong, H. Yang, Q. Wang, Q. Zhang, Y. Zhu, H. Wang and Q. Shen, *Chem. Eng. J.*, 2019, **361**, 1-11.

6 J.-F. Zhang, Y. Wang, X. Shu, C.-P. Yu, M.-F. Xiao, J.-W. Cui, Y.-Q. Qin, H.-M. Zheng, Y. Zhang, D. Chen, P. M. Ajayan and Y.-C. Wu, *Sci. Bull.*, 2018, **63**, 322-330.

7 S. Jiang, M. Pang, J. Zhao, B. Xing, Q. Pan, H. Yang, W. Qu, L. Gu and H. Wang, *Chem. Eng. J.*, 2017, **326**, 1048-1057.

8 W. Song, J. Wu, G. Wang, S. Tang, G. Chen, M. Cui and X. Meng, *Adv. Funct. Mater.*, 2018, **28**, 1804620.

9 H. Fan, X. Zhang, Y. Wang, J. Lang and R. Gao, *J. Power Sources*, 2020, **474**, 228603.

10 Z. Wang, J. Chang, L. Chen, Y. Li, D. Wu, F. Xu, K. Jiang and Z. Gao, *Electrochim. Acta*, 2019, **323**. 134815.

11 Q. Wang, Y. Luo, R. Hou, S. Zaman, K. Qi, H. Liu, H. S. Park and B. Y. Xia, *Adv. Mater.*, 2019, **31**, e1905744.

12 J. Ye, X. Zhai, L. Chen, W. Guo, T. Gu, Y. Shi, J. Hou, F. Han, Y. Liu, C. Fan, G. Wang, S. Peng and X. Guo, *J. Energy Chem.*, 2021, **62**, 252-261.

13 F. Shi, S. Zhao, J. Yang, Y. Tong, J. Li, S. Zhai, X. Zhao, S. Wu, H. Li, Q. An and K. Wang, *J. Mater. Chem. A*, 2022, **10**, 12679-12691.

14 Y. Lin, K. Sun, S. Liu, X. Chen, Y. Cheng, W. C. Cheong, Z. Chen, L. Zheng, J. Zhang, X. Li, Y. Pan and C. Chen, *Adv. Energy Mater.*, 2019, **9**, 1901213.

15 A. Meng, X. Yuan, T. Shen, Z. Li, Q. Jiang, H. Xue, Y. Lin and J. Zhao, *J. Mater. Chem. A*, 2019, **7**, 17613-17625.

16 J. Zhao, Z. Li, T. Shen, X. Yuan, G. Qiu, Q. Jiang, Y. Lin, G. Song, A. Meng and Q. Li, *J. Mater. Chem. A*, 2019, **7**, 7918-7931.

17 Y. Huang, L. Quan, T. Liu, Q. Chen, D. Cai and H. Zhan, *Nanoscale*, 2018, **10**, 14171-14181.

18 J. Sun, J. Wang, Z. Li, L. Niu, W. Hong and S. Yang, *J. Power Sources*, 2015, **274**, 1070-1075.

19 L. Li, X. Zhang, Z. Zhang, M. Zhang, L. Cong, Y. Pan and S. Lin, *J. Mater. Chem. A*, 2016, **4**, 16635-16644.

20 D. Ying, Y. Li, R. Ding, W. Shi, Q. Xu, Y. Huang, Z. Jia, W. Yu, X. Sun, P. Gao, E. Liu and X. Wang, *Adv. Funct. Mater.*, 2021, **31**, 2101353.

21 Y. Lin, K. Sun, S. Liu, X. Chen, Y. Cheng, W. C. Cheong, Z. Chen, L. Zheng, J. Zhang, X. Li, Y. Pan and C. Chen, *Adv. Energy Mater.*, 2019, **9**, 1901213.

22 Y. Tang, H. Shen, J. Cheng, Z. Liang, C. Qu, H. Tabassum and R. Zou, *Adv. Funct. Mater.*, 2020, **30**, 1908223.

23 Y. Zhao, L. Hu, S. Zhao and L. Wu, *Adv. Funct. Mater.*, 2016, **26**, 4085-4093.

24 S. Liu, S. C. Lee, U. Patil, I. Shackery, S. Kang, K. Zhang, J. H. Park, K. Y. Chung and S. Chan Jun, *J. Mater. Chem. A*, 2017, **5**, 1043-1049.

25 H. B. Li, M. H. Yu, F. X. Wang, P. Liu, Y. Liang, J. Xiao, C. X. Wang, Y. X. Tong and G. W. Yang, *Nat. Commun.*, 2013, **4**, 1894.